Si–C/G based anode swelling and porosity evolution in 18650 casing and in pouch cell

Delphine Vidal, Côme Leys, Benoit Mathieu, Nicolas Guillet, V. Vidal, Daniel Borschneck, Perrine Chaurand, Sylvie Genies, Eric de Vito, Michal Tulodziecki, et al.

Si-C/G based anode swelling and porosity evolution in 18650 casing and in pouch cell

Delphine Vidal[a], *Côme Leys*[a], *Benoit Mathieu*[a], *Nicolas Guillet*[a], *Vladimir Vidal*[b], *Daniel Borschneck*[b], *Perrine Chaurand*[b], *Sylvie Genies*[a], *Eric De Vito*[a], *Michal Tulodziecki*[c], *Willy Porcher*[a,*]

[a] University Grenoble Alpes, CEA-Liten, F-38054 Grenoble, France

[b] Aix Marseille Univ, CNRS, IRD, INRAE, Coll France, CEREGE UMR 7330, Aix en Provence, France

[c] Umicore Research, B-2250 Olen, Belgium

* Corresponding author.
E-mail address: willy.porcher@cea.fr

Abstract

Silicon lithiation induces a high material expansion which leads to significant swelling and mechanical pressure at the anode and cell level. In this study, the effect of the various mechanical constrains on the swelling behaviour of pouch cell and cylindrical cell (18650) with high performance silicon carbon graphite (Si-C/G) anode material was evaluated. In case of 18650 cells, strain gauges were used to evaluate the strains and pressure generated from anode swelling during cycling process; in addition, individual cell components thickness change was captured at 8 different states of charge (SOC) during a cycle by *in situ* 3D imaging with X-Ray micro computed-tomography (voxel size 1.6µm) combined with a specific image treatment. For bi-layer pouch cells, *operando* swelling was measured using an in-house high precision (< 0.1µm) compression set-up with simultaneous pressure and thickness recording as well as dynamic pressure regulation system. Combining these unique experimental techniques and the modelling of Si-C/G active material swelling in function of the SOC we were able to provide insights in porosity changes of anodes for the two cell formats.

Keywords

Lithium-ion battery, silicon anode, compression set-up, X-ray micro computed-tomography, strain gauge

1. Introduction

The strong demand for electric mobility is driving the frenetic development of battery production lines installation with ever-greater scales and robotization. These gigafactories have enabled production costs to fall at the cell level. On the other hand, active material structures have changed very little since the first commercial in 1991[1]. At the cathode side, the $LiCoO_2$ lamellar material has shown substitution of the transition metal by high content of Ni (up to 90%) and Mn or Al leading to $LiNi_xMn_yCo_zO_2$ (NMC) or $LiNi_xCo_yAl_zO_2$ (NCA) materials. At the anode side, graphite is still dominant with introduction of silicon oxide as additive from 2013, typically with 2 wt. %. The anode active materials evolution was not the main driver of the energy density increasing but much more the inactive material proportion decrease and the end of charge voltage cut-off increase.

However, the introduction of silicon at the anode represents a significant potential for improvement. This improvement is as high as 10, 20 and even 30% in terms of volumetric energy density with silicon proportions in the anode of 6, 14 and 40%, respectively. This theoretical estimation is based on thick and dense anode with high active material content and low irreversible first cycle[2]. Numerous works suggest interesting solutions in terms of material design, electrode binders, or electrolyte composition[3,4]. Nevertheless, the high swelling of silicon of 280% during lithiation remains a challenge, not only for the stability of the solid electrolyte interphase (SEI) at particle level but also for the anode thickness variations at the cell level.

The study of swelling during the alloying of silicon with lithium is undoubtedly associated with the works of Jeff Dahn *et al.* starting in 2001[5] by “Colossal reversible volume changes in lithium alloys” observed by *in situ* atomic force microscopy (AFM) on alloy films. In 2003, using continuous and patterned films of alloy electrodes and still by *in situ* AFM, they proposed that silicon swelling was linear, reversible and closed to 300%[6]. More recently in 2017, they followed the volume expansion by *in situ* pressure measurements of pouch cells with NCA or LCO cathodes and SiO-G, Si alloy-graphite or nano Si-C anodes[7]. They explained the asymmetric nature of the volume expansion in charge and discharge is a consequence of the different active materials in the cells, with linear swelling of silicon,

the particular 2L-2 staging of graphite which does not induce volume variation and NCA contraction at the end of charge.

Based on this approach, we propose in this work to compare the porosity evolution at anode level when cycling in pouch cell at various constant pressures and in cylindrical hard casing. Different groups have already investigated the pressure impact on cell capacity retention[8–12] or the anode morphology evolution[13,14]. It is generally assumed that active material expansion leads to both anode swelling and porosity accommodation, which generate stress on other components[7,15–17] and anode cracks and delamination[18,19]. However, it is still poorly understood how this swelling takes place in the porous structure of the electrode during cycling, and how electrodes materials are affected. In particular, some studies conclude that the separator morphology evolution could be responsible of the accelerated degradation at the anode side.

In this study, compared cells (bi-layer pouch cell and 18650 cylindrical cell) are composed of the same electrodes with NMC622 cathode material and silicon carbon composite blended with graphite (Si-C/G based anode) to have a reversible specific capacity of 500 $mAh.g^{-1}$ for the anode. Capacity retention and resistance evolution are presented in a first part for different cells conditions. The modelling of the active materials volume expansion as a function of the state of charge (SOC) is then described.

To follow the electrode thickness evolution in pouch cell with a pressure of 0.1 and 1 MPa, we have developed an *operando* compression set-up with highly planar conception and high sensitivity of the sensors, having a final precision of 100 nm. In parallel, we have performed 3D imaging by X-ray micro computed-tomography (micro-CT) analysis on the same 18650 cylindrical cell at different states of lithiation (SOL) using last generation of 3D imaging equipment and a deep image analysis to study the *in situ* variation of electrode and separator thickness. Gauges were fixed on the rigid casing to take into account its deformation. The global anode porosity is finally extracted for all the cells cycled at constant volume or constant pressure from experimental swelling measurements and active material swelling modelling.

1. Experimental procedures

1.1. Electrode preparation

The Si-C/G anode was formulated with 90% of active material (mixture of silicon carbon composite with silicon particles inside carbon matrix (Umicore, D_{90}=30 µm) and graphite (Hitachi, D_{50}=21 µm) to reach 500 mAh.g^{-1} reversible discharge capacity), 2 wt. % carbon black or CB (C65 from Imerys), 1 wt. % vapour grown carbon fibres or VGCF and 7 wt. % of Na-PAA (from Aldrich) as binder. More details on electrode preparation are presented in supporting information. All electrodes' properties are summarized in Table 1.

Table 1: Electrode's loadings, thicknesses, porosities and areal capacities.

	Cathode		**Anode**	
	One-side coated	Double-side coated	One-side coated	Double-side coated
Loading (mg.cm^{-2})	16.5	16.4	6.3	6.2
Areal total capacity (mAh.cm^{-2})	2.9	2.9	3.3	3.2
Areal reversible capacity (mAh.cm^{-2})	2.6	2.6	2.84	2.8
Thickness with Al or Cu foil (µm)	79	136	58	105
Porosity (%)	32	33	38	40

1.2. Test cells

Different cell definitions are presented in supporting information.

1.3. Test procedure

1.3.1. Electrochemical tests

After a 2h rest, all full-cells (with NMC622 cathode) were formed at C/20 up to 4.2 V and next discharged to 2.5 V at C/20 in a climate chamber at 45°C. The 2nd and 3rd formation cycles were performed at room temperature in the same voltage condition at C/10 and C/5, respectively. Each charge step was ended by a floating voltage step up to hold down to current of C/50.

Additional cycles for various testing were completed at room temperature with the same voltage and a floating step conditions. Current rates and state of charge (SOC) were calculated based on the capacity measured during the first cycle at C/5 post-formation.

Formation for half-cells (with Li metal) was performed after a rest of 4h and consisted of one cycle at C/20 and 2 cycles at C/5. A third cycle at C/5 was performed for dQ/dV analysis. Each lithiation step was followed by a floating step up to hold down a current of C/100 and every cycle was performed at room temperature. A voltage window of 0.01V to 1V was used for graphite and silicon-carbon composite whereas a voltage window of 0.05V to 1V was used for silicon in order to avoid formation of the $Li_{15}Si_4$ crystalline phase.

1.3.2. Compression setup for bi-layer pouch cell

The testing of pouch cell was conducted under constant pressure of 0.1 MPa and 1 MPa in a flexible compression mode.

For electrochemical cycling, two calibrated clips applying 100N on 10cm² surface of cathode were used to impose 0.1 MPa whereas a calibrated spring with a lever arm effect was used to apply 1 MPa. Those tools exhibit a theoretical force variation of 0.3% for a maximum expansion of 30% of the anode holding the pressure constant during electrochemical testing.

For swelling measurement, an in-house operando compression set-up presented in Figure S1 was designed. The set-up is composed of a dynamic pressure regulation system from 0.05 to 10 MPa and records simultaneously pressure and thickness. It was designed with highly planar conception and high sensitivity of the thickness sensors, having a precision of 100 nm. 3 linear variable differential transformers are placed around the samples to measure the thickness changes and correct an eventual flatness issue. Low pressure tests were always performed before high pressure tests in order to avoid possible irreversible changes in the electrode microstructure due to higher pressure.

1.3.3. Strain gauge

A 45° rectangular single-plane rosette strain gauge (C2A-06-125LR-120 from MICRO-MEASUREMENT) was used in order to measure the main strains of the 18650 casing and assess the rigidity of its hard metal casing (**Erreur ! Source du renvoi introuvable.**).

Considering the casing material as homogeneous in composition, having isotropic mechanical properties and stress proportional to strain, Hooke's law can be used to convert the principal strains Ep and Eq into principal stresses σ_p and σ_q. Knowing the elastic modulus E and the Poisson's ratio ν, the Hooke's law for biaxial stress state can be expressed as follow:

(1) $\sigma_p = \frac{E}{1-\nu^2}(Ep + \nu Eq)$ and $\sigma_q = \frac{E}{1-\nu^2}(Eq + \nu Ep)$ with $E_{steel} = 205\ GPa$ and $\nu_{steel} = 0.29$

Finally, the thin-walled pressure vessel theory gives the following relation for our cylindrical casing:

(2) $\sigma_\theta = \frac{P.r}{t}$

With the circumferential stress σ_θ, the internal pressure P, the inner radius r and the thickness of the casing t.

1.3.4. *In situ* 3D imaging by X-ray micro-CT

Micro-CT, a non-destructive 3D imaging technique, was used to *in situ* determine electrodes and separator thickness evolution with SOC in cylindrical hard casing (18650 format).

1.3.4.1. 3D image acquisition

The same cylindrical cell was 3D-scanned using a Zeiss microXCT-400 system during a charge/discharge cycle. All scans were acquired at 140 kV and 10W (W target). After formation, the whole cylindrical cell was first quickly scanned in large field-of-view (LFOV) with an isotropic voxel size of 42.4 µm using the x0.4 magnification optical objective. From this LFOV scan, a volume of interest (VOI) was selected for high-resolution imaging (Figure S3). The x10 objective was then used to achieve an isotropic voxel of 1.6 µm and a VOI of 1.6x1.6x1.6 mm^3. A total of 2001 projections were collected through 360° rotation with an exposure time of 60 s per projection, for a total acquisition time of 38 hours (Figure S3a). This acquisition time being very long, *operando* measurement was impossible, thus scans were performed at 8 various SOCs upon one cycle. Floating steps up to C/100 were performed at each chosen SOC before scanning in order to study an electrochemically stable state of the battery.

High-resolution 3D imaging at micrometre-scale is required to distinguish the various components in the cell and to measure their thickness variation during charge/discharge cycle (Figure S3b).

1.3.4.2. 3D image reconstruction and analyse

Volume reconstruction was performed with XMReconstructed-Parallel Beam-9.0.6445 software using a filtered back projection algorithm.

The histogram of the reconstructed volume represents the X-ray absorption in each voxel (expressed as an arbitrary Gray Scale Value, GSV) as function of the number of voxels for each GSV (intensity). The GSV depend on material composition (density) and thickness.

The Fiji free software was then used to analyse the reconstructed volumes[22]. A specific image processing procedure was developed to determine thickness of each component and is described in the Results part.

2. Results & discussion

2.1. Electrochemical behaviour of Si-C/G composite anode

The active material of the anode is a blend of a silicon carbon composite with graphite. The electrode contains 90 wt. % of active material and has a global reversible specific capacity of 500 $mAh.g^{-1}$. The electrochemical behaviour of the anode in half-cell is presented in Figure 1a. The 4^{th} cycle was chosen to avoid considerations of the first cycle with silicon irreversible amorphization. Graphite and pure silicon materials behaviours are also reported in this Figure 1a with half-cell evaluation in the same conditions in order to identify electrochemical contributions in this blended anode. The Si-C/G composite anode shows a mixed behaviour with three peaks in delithiation between 70 and 250 mV corresponding to phase transitions in graphite[23] and a sharp peak around 0.45 V corresponding to $Li_{15}Si_4$ crystallized phase delithiation[24,25]. The anode contained in total around 6.5 wt. % of silicon.

For the pure silicon electrochemical behaviour reported in Figure 1a, a second peak can be observed at around 280 mV corresponding to amorphous Li_xSi phase delithiation[26]. The presented electrochemical behaviour of pure silicon does not show full crystallization as the lithiation is stopped at 50 mV. This electrochemical behaviour is representative to what happens in a Li-ion cell and will be useful for further calculation. Indeed, $Li_{15}Si_4$ crystallisation do not occur in a typical Li-ion cell

configuration as the cell balancing is of 1.10 and Li loss happens at the first cycle. Moreover, it is noteworthy that the lithiation of both silicon and graphite happens simultaneously in the anode whereas delithiation occurs first for graphite at low potential considering half-cell configuration and then for silicon at higher potential as already reported in literature[27,28]. It means that, for a given potential, graphite state of lithiation (SOL) will be different from silicon SOL and from Si-C/G anode SOL. The SOL of both materials in the Si-C/G anode was estimated from pure graphite and silicon potential behavior at the 4^{th} cycle considering 6.5 wt.% of silicon, and 83.5 wt.% of graphite in the formulation. Potential of the Si-C/G anode in the Figure S4 fits pretty well at low potential and is quite different regarding silicon contribution especially in delithiation. Pure silicon anode does not crystallize and also carbon not fully graphitized in the composite should explain that higher capacity is obtained between 500 and 700 mV vs Li^+/Li in delithiation or 300 and 700mV vs Li^+/Li in lithiation. The obtained SOL of both materials in the anode is plotted for the fourth cycle on Figure 1b. The anode specific capacity considered is the one actually used in Li-ion cell design having a balancing of 1.10 and an irreversible capacity loss at the first cycle of 13%. This is the reason why the reversible anode specific capacity considered here is of 442 $mAh.g^{-1}$. Lithiation of the anode starts mainly with silicon lithiation until 100 $mAh.g^{-1}$ followed by a lithiation of both materials with quite similar pace keeping silicon SOL at higher values than graphite SOL and finally reaches an equal SOL of 86% which is a fortunate coincidence. The delithiation profile is strongly different with graphite delithiation starting up to 24% SOL before silicon significantly starts to delithiate. This result matches what can be found in literature[7,27]. Obviously, each material will undergo different volume changes relative to their respective SOL in the composite anode.

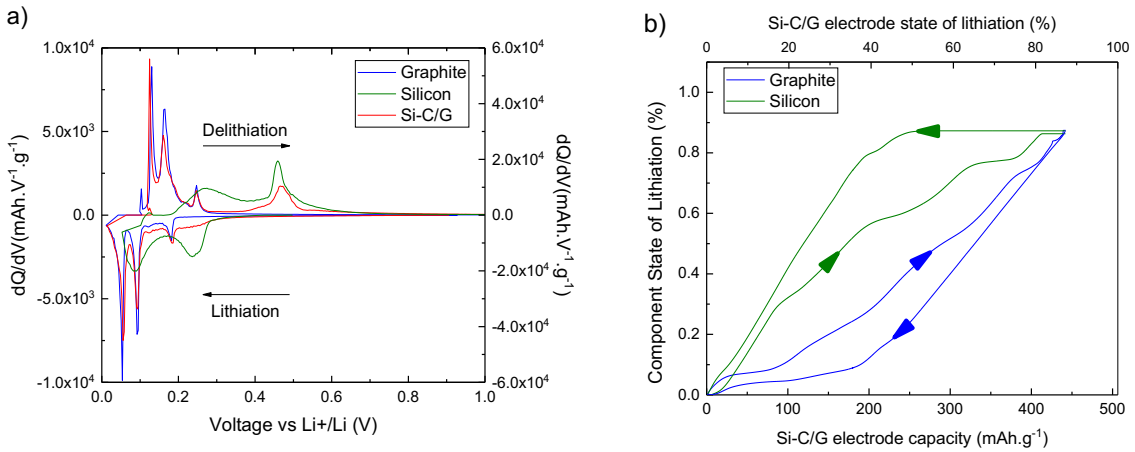

Figure 1: a) Incremental capacity at C/5 and RT of half-cells with working electrodes containing graphite (blue), Si-C/G composite anode (red) and silicon electrode (green) after 3 cycles of formation. Potential profiles are shown in SI (Figure S4a). b) Component's state of lithiation vs composite capacity in full-cell configuration. Arrows show lithiation/delithiation cycle.

Cycle life of NMC622 based cathode versus Si-C/G based anode was evaluated in 18650 cells of 2 Ah and 170 Wh.kg^{-1} at C and in pouch cells of 27 mAh at C/2 when applying a constant pressure of 0.1 MPa or 1 MPa. For these cycling tests, a C/5 cycle is done every 20 cycles with a resistance measurement at 50% SOC with a 30s pulse at 2C. Results obtained for cycles at C/5 presented on Figure 2a are representative of one of the three cells (not shown) which have demonstrated very good reproducibility. In 18650 cells, pressure was not controlled and was generated internally as it will be presented later in the paper.

The normalized capacity evolution in 18650 cells seems more stable with 90% and 80% of the initial capacity recovered at C/5 after 220 and 420 cycles at 1C, respectively. The pouch cells have very similar capacity retention for both applied pressures, with 80% of the initial capacity after 310 cycles at C/2. Concerning resistance evolution higher initial resistance is observed for 18650 cells with also stronger increase upon cycling. Regarding pouch cells results, similar initial resistance is measured for both applied pressure whereas lower pressure leads to lower resistance during extended cycling. Considering that the resistance is measured for a 30s pulse at 2C, electrolyte conductivity limitation is usually observed. A first explanation could be that a high pressure leads to a lower electrodes and separator thickness. This is associated with ionic pore resistance and charge transfer resistance increasing for both electrodes and separator, finally increasing the overall cell resistance[29]. However,

such decreased ion mobility does not seem to impact the cycle life which even shows a slightly better capacity retention when higher pressure is applied. This could be linked to a more resilient electronic conduction network to keep particles connected while SEI layer is growing upon cycling.

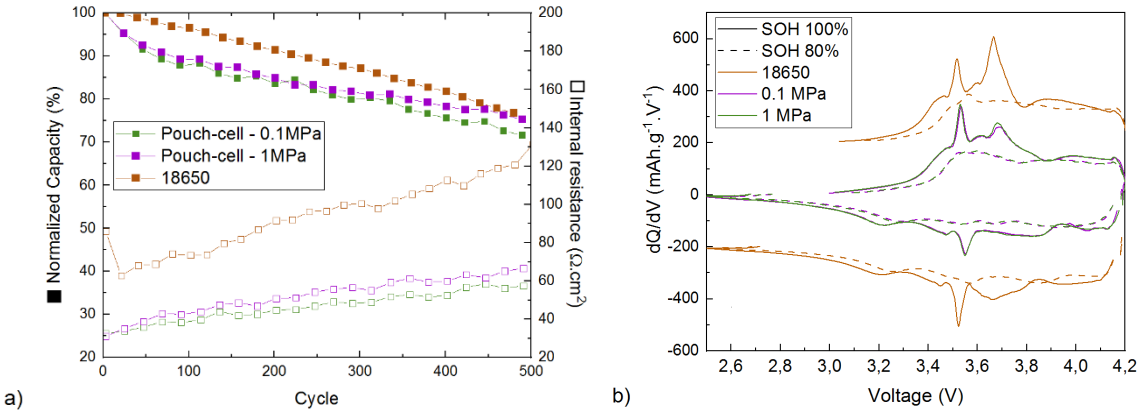

Figure 2: a) Normalized discharge capacity for cycles at C/5 and resistance (2C, 30s at 50% SOC) evolution upon cycling of 18650 cells at C and pouch cells at C/2 under constant pressure of 0.1 MPa and 1 MPa b) incremental capacity at state of health (SOH) of 100% (1st post-formation cycle) and 80% (after 310 and 420 cycles for pouch and cylindrical cells, respectively) for various cells. SOH is defined as the capacity retention at C/5 in comparison to initial capacity at C/5. 18650 cell plots are shifted to +200 in charge and -200 mAh.g-1.V-1 in discharge to ease reading the curves.

Differential capacity as a function of the voltage of the full-cells at 100% and 80% SOH are plotted on Figure 2b in order to give some insight on the origin of the capacity fade. The peaks on the fresh cell at ~3.7 V in charge and at ~3.6 V in discharge correspond to redox transitions of NMC622[30]. For the negative electrode, the peaks observed at ~3.55 V in charge and discharge corresponds to Li (de)intercalation in graphite[31] while the peak at 3.15 V in discharge that could be attributed to silicon dealloying. A global attenuation of the peaks and smoothing of the curve is visible after 420 cycles, which is certainly linked to lithium loss and heterogeneity appearing in the electrode. In addition, peaks shift to higher voltage, indicating an increase of both electrode resistance, which is consistent with the increasing resistance measured for the full-cell. However, silicon is still significantly active with low loss of active material after 420 cycles. The main degradation appears to be related to lithium trapping,

typically due to SEI growing at the anode during repeated the contraction/expansion cycles. However, materials appear to be still electrochemically active and silicon particles successfully connected.

2.2. Swelling behaviour of full-cell containing Si-C/G composite anode and NMC622 cathode

Each component SOL and their respective volume change at a given SOC can be combined to determine the swelling of each electrode of a bi-layer full-cell considering the following assumptions:

- Cells were designed with a balancing superior to 1.10 meaning that none of the negative electrode components can access their full capacity, therefore no component was ever 100% lithiated. In particular, the lithiated crystalline phase $Li_{15}Si_4$ was never fully formed and a model using 0.05V as lower voltage cut-off is appropriate[26,32];
- The cut-off voltage at 4.2V in full-cell corresponds to a relative change of crystallographic unit cell volume smaller than 1.5% for NMC622 particles[33] (see Figure S5);
- Amorphous silicon undergoes a 280% linear and reversible volume expansion/contraction during post formation lithiation/delithiation process[6,26]. No plastic deformation of silicon is considered;
- Graphite and carbon undergo a 10% linear and reversible swelling during lithiation/delithiation with a plateau between 25% and 50% of lithiation corresponding to phase transformation 2L→2[23] (see Figure S5);
- Binder and electronic conductors' volume are considered constant during formation and post-formation cycling. No porosity or microstructural rearrangements are accounted for,
- The SEI thickness being generally reported of nanometre scale[34–37], it is negligible for first post-formation cycles;
- No external stress is applied, and pores volume is considered constant, meaning that porosity will decrease theoretically during materials expansion.

Anisotropic volume change in the direction perpendicular to the current collector is considered only as expansion/contraction of the electrode takes place mainly in the transversal direction[38]. Hence,

there is a linear equation (3) between the electrode volume and its thickness where S is the surface and remains constant, and h is the average thickness. The total thickness of the Si-C/G electrode can be expressed as function of all solid phases and porosity proportions in equation (4). Each solid phase contribution in the pristine electrode is obtained from the proportion in the formulation, *d* the solid phase density and *l* the electrode loading (5). Finally, the thickness change at different SOL is the sum of the thickness variation of all active materials at this SOL as the thickness attributed to porosity and inactive components are considered constant (6). Graphite and silicon swellings are calculated according to literature reported in Figure S5 or by equation from (6a) to (6d).

(3) $V_{electrode} = S \times h_{electrode}$

(4) $h_{electrode} = h_G + h_{Si} + h_{binder} + h_{EC} + h_{SEI} + h_{pores}$

(5) $h_{i,SOL=0\%} = \frac{wt\%_i}{d_i} \times l$

(6) $\Delta h = \Delta h_G + \Delta h_{Si}$ with:

a. $\Delta h_G = h_{G,SOL=0\%} \times (1 + 0.2 \times SOL_G)\ for\ graphite\ SOL\ from\ 0\ to\ 25\%$

b. $\Delta h_G = 1.2 \times h_{G,SOL=0\%}\ for\ graphite\ SOL\ from\ 25\ to\ 50\%$

c. $\Delta h_G = h_{G,SOL=0\%} \times (1 + 0.1 \times SOL_G) for\ graphite\ SOL\ from\ 50\ to\ 100\%$

d. $\Delta h_{Si} = h_{Si,SOL=0\%} \times (1 + 2.8 \times SOL_{Si})$

The calculated swelling of the Si-C/G composite electrode and the full-cell containing this anode and a NMC622 cathode after formation during the 4th cycle is presented in Figure 3. Input data of the model are the state of lithiation of graphite and silicon material presented in the Figure 1b and the parameters of the bi-layer pouch cell presented in the Table 1 in order to have relevant comparison with experimental swelling data presented thereafter.

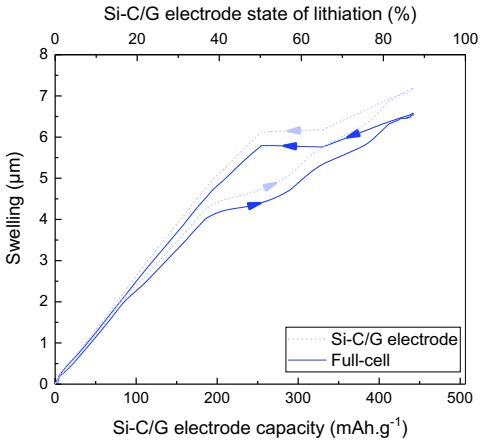

Figure 3: Modelled swelling of the Si-C/G composite anode and a bi-layer pouch cell containing the same anode and an NMC622 cathode, during one cycle at C/5 post formation.

The awaited total anode expansion is about 26.5% with 18.2% due to silicon material and 8.3% attributed to graphite. Considering the effective balancing of 1.10, the calculated electrode thickness increases by 7.21 µm corresponding to 24.3% expansion of the active anode layer as we do not consider full lithiation. Regarding the swelling profile, the slope depends on the state of lithiation of both materials and on their respective swelling profiles. With a swelling of 280%, silicon lithiation/delithiation corresponds to sharper slopes than graphite that undergoes an expansion of 10% when lithiated. During lithiation, silicon is the main active material up to 100 $mAh.g^{-1}$ with sharp slope, followed by a mixed behaviour of graphite and silicon for the rest of lithiation with a plateau corresponding to 2L->2 phase transition in graphite between 180 and 280 $mAh.g^{-1}$. During discharge, two distinct regions are shown: a first one between 450 and 250 $mAh.g^{-1}$ with only graphite delithiation and the 2L->2 phase transition between 330 and 250 $mAh.g^{-1}$ followed by a second one with a sharp slope corresponding to silicon delithiation.

In full-cell configuration, the cathode contraction effect is limited, reducing by 0.63 µm the overall expansion, and having no impact on the global swelling profile. Therefore, full-cell swelling is mainly due to Si-C/G anode contribution.

This simulated expansion will now be compared to experimental results upon one charge/discharge cycle of a pouch cell swelling from *operando* compression setup and *in situ* thickness measurements

of the anode inside an 18650 cylindrical cell from 3D imaging. In order to deeper understand cell design or pressure impact on the electrode microstructure, the Si-C/G electrode porosity will be estimated by subtracting computed values from experimental data of swelling.

(7) $Porosity = \frac{h_{pores}}{h_{electrode}}$

(8) $\Delta h_{pores} = \Delta h_{electrode} - \Delta h_G - \Delta h_{Si}$

2.3. Swelling of pouch cells under constant applied pressure

Figure 4a shows *operando* swelling measurement of the same pouch cell under a controlled constant pressure of 0.1 MPa then 1 MPa for 3 consecutive cycles at a low C-rate of C/5.

The stabilized initial thickness of the total pouch cell after applying 0.1 MPa is 377.8 µm. Three formation cycles are firstly applied at respectively C/20, C/10 and C/5 with a pressure of 0.1 MPa before recording the 4th cycle at C/5 and 0.1 MPa. The initial thickness of the 4th cycle is of 385.6 µm, indicating an irreversible thickness increase of 7.8 µm during formation step of the cell, which can be related to particle rearrangement and a lack of pressure to recover the compactness of the particles stacking after swelling. If assigned to anode expansion only, this represents an increase of +15.6% of the active layer. The swelling is not entirely reversible with still +0.9 µm, +0.5 µm and +0.4 µm of deviation for the initial thickness of the 4th, 5th and 6th cycles presented which might be due to a pressure too low to come back at the initial anode thickness. However, compared with the simulated or modelled swelling in Figure 4b, similar amplitude during a post-formation cycle of 6.3 µm for the experimental swelling is observed validating our assumptions of part 2.2 and meaning the anode pores volume should not be overly impacted during lithiation/delithiation cycles under this pressure.

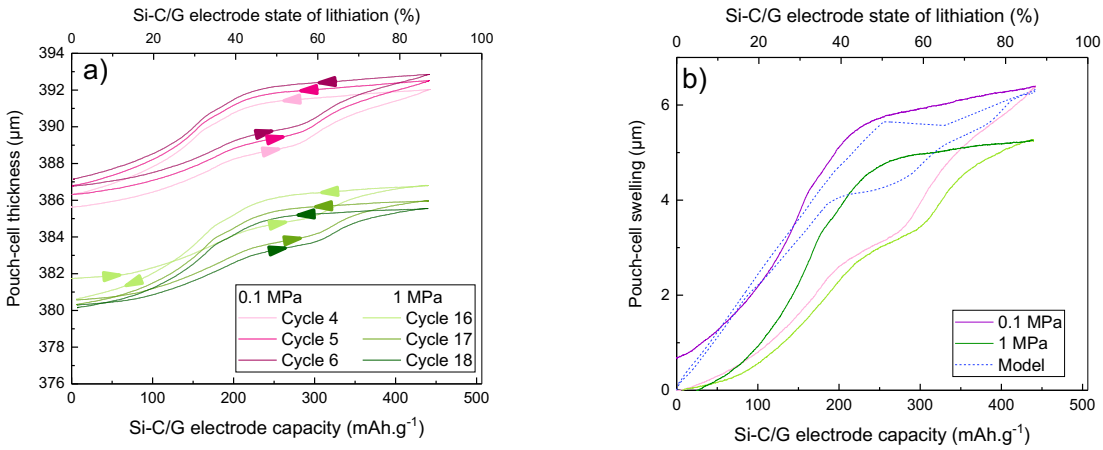

Figure 4: a) Total swelling of the same bi-layer pouch cell under 0.1 MPa and then 1MPa during post-formation cycles at C/5; b) corresponding relative thickness change during the 4th and 17th cycle comparison with the modelled swelling of a bilayer pouch cell presented Figure 3.

Moreover, some similar features can be spotted especially the alternation of intercalation in graphite and alloying of silicon during charge of the cell. Also, the two different slopes in discharge fairly confirm that graphite is firstly delithiated. Two main differences with the modelled swelling are spotted. One concerns graphite 2L -> 2 phase transition which is not so visible in discharge. This could be explained by graphite particles not being homogeneously delithiated in the electrode, smoothing the swelling. The other discrepancy is the smaller experimental swelling than expected during the whole lithiation. One explanation could be a change in porosity accommodating particles swelling. Another one could be the fact that our model only considers 1D expansion which is not truly representative of the complex real swelling occurring at particles level, with particle-particle friction and rearrangement. Finally, it could be related to the design of Si-C composite which partially suppresses the Si expansion.

When the pressure applied increases to 1 MPa, a drop of 5.4 µm is observed with a stabilized thickness of 381.7 µm at beginning of the 16th cycle. This contraction is probably due to particles rearrangement in the electrodes along with separator contraction as the pressure is significantly higher than the one applied in the previous test. It should be noted that cycles 7 to 15 (not shown here) are perfectly reversible and do not participate in this thickness change. The first charge under 1 MPa shows the same alternating silicon/graphite lithiation with a swelling amplitude of 5 µm. Contrary to cycles under

low pressure, the first discharge under 1 MPa presents a higher contraction amplitude than expansion amplitude with an irreversible swelling of -1.1 µm but a similar reversible capacity. The following 17th and 18th exhibit a behaviour closer to the one under 0.1 MPa. Main differences are a swelling amplitude decreased to 5.3 µm and a small irreversible compression of 0.3 µm and 0.1 µm instead of expansion at each cycle. Both phenomena can be linked to the higher applied pressure limiting the anode expansion during charge, especially for capacities higher than 300 mAh.g^{-1} and accompanying its contraction during discharge. This behaviour is more pronounced during the first cycle after pressure change, where the majority of particle rearrangements due to higher pressure takes place during discharge. It is important to notice that the more reversible swelling is not necessarily correlated with some discontinuous SEI formation. In fact, because of the limited vertical expansion imposed by the applied pressure, graphite and silicon particles will have to expand by filling the pores of the electrode which will also be filled by continuous SEI growth to a lesser extent. A great impact on porosity is expected and will be calculated hereafter for both pressures.

Supplemental measurements were performed to address contribution of the pouch bag and separator in order to calculate the porosity change (Figure S6). Results show that the compression of one layer of pouch bag is of 0.25 µm, 1.46 µm and 2.47 µm at 0.1, 1 and 6 MPa after 8h with an initial thickness of 110 µm. One layer separator with an initial thickness of 20 µm, shows a compression of 0.04 µm, 0.23 µm and 1 µm at 0.1, 1 and 6 MPa respectively. The porosity decrease can be calculated to less than 1% for 0.1 and 1 MPa and of 3% at 6 MPa on the 39% initial porosity and should not significantly impact the lithium conductivity.

2.4. Swelling of the jellyroll inside a constrained volume

2.4.1. Rigidity of the hard metal casing

To evaluate components thickness evolution of cylindrical hard casing in 18650 format due to the anode swelling during lithiation/delithiation, a preliminary study focuses on the investigation of the casing deformation during successive charge discharge cycles. To that end, information on the main

strains of the casing Ep and Eq and their orientation were collected using a rosette strain gauge. Results obtained using equations (S1), (S2), (S3), (1) and (2) for the 3 cycles of the formation protocol and three additional cycles at C/10 are presented on Figure 5a. Because the measured deformation takes place in a cylindrical coordinate system, the calculated main strains Ep and Eq are in axial and orthoradial direction respectively (Figure 5a). The temperature dependence of the measured strains has been studied in a preliminary study and all data are corrected in order to only observe the strain variation due to electrochemical processes. As the internal void between the jelly roll and the casing in the z-direction is quite important and also because the negative electrode is expanding in the direction perpendicular to the current collector[6,15], it is consistent to observe a larger amplitude for the orthoradial strain Eq than for axial strain Ep. However, we do not explain the negative sign of the strain of Eq. Preliminary test has shown positive and negative strains of Eq when temperature is increased and decreased, respectively, but it is evident that Eq must be positive during anode expansion. The axial strain Ep is globally positive and follows Eq variations.

During the formation step with 3 cycles and an increasing C-rate, a rise of the maximum and minimum strains for each cycle is observed. For the next 3 cycles, maximum strains continue to slightly increase but the hoop strain amplitude reaches a steady value of 600 µm.m^{-1} corresponding to 0.06% or 10 µm variation of the cell diameter. This very low strain amplitude value allows us to assume that the metal casing is stiff, and that anode materials expansion is exclusively accommodated inside the constant volume of the steel case. Also note that the same number of 3 cycles is necessary to stabilize the mechanical behaviour as observed for pouch cells when applying a constant pressure. With negative values and variations opposite to those observed in the literature[39–41], we chose to use a factor -1 for further calculations in order to observe an increase of the strain in charge and a decrease in discharge.

The corresponding pressure P can be calculated from the mains strains Ep and Eq via principal stresses σ_p and σ_q calculation using equations (1) and (2). The relationship between strains, stresses and pressure being linear, the radial pressure curves is very similar to the hoop strain curve Eq. During 3

formation cycles, the maximum pressure (observed at 100% SOC) increases until it reaches a steady value of 4.5 MPa for the next cycles, as shown in Figure 5b for the 4th cycle. The silicon and graphite swelling added to SEI formation takes place inside a constrained volume fixed by the rigid casing imposing high pressure over the jellyroll. At the end of formation, the pressure in discharged state is of 0.3 MPa and is related to particles rearrangement which is associated to an irreversible expansion of the jellyroll.

The shape of the pressure measurement in Figure 5b shows that the expansion is neither linear nor symmetrical with the state of lithiation of the negative electrode revealing a hysteresis between charge and discharge. Before 25% SOL of the anode, low pressure is observed. This might come from porosity being high enough to accommodate particle swelling. At higher states of anode lithiation, the pressure can be correlated to graphite and silicon SOL in the electrode presented earlier. During charge, as observed previously, graphite and silicon lithiation happens simultaneously with a slope related to the active material being simultaneously lithiated, the highest slope being associated to silicon, typically between 60 and 70% of SOL. The slight pressure drop at the end of charge (98% SOC) corresponds to the floating step: with decreasing C-rate, Li^+ diffusion in the electrode is no longer limited[42,43]. Consequently, the lithium concentration inside the negative electrode tends to homogenise between Si-C and graphite particles, causing a relaxation of the constraints inside the electrode. During discharge, two distinct regions are shown: a first one between 100% and 45% SOL with a steady slope corresponding to graphite delithiation, and a second one after 45% SOL with a sharper slope corresponding to silicon delithiation. Finally, although the evolution of pressure is different from the variation of thickness, similarities are evident as a result of the different variations of SOL of graphite and silicon in charge and in discharge.

It should be noted that cathode and separator contraction could also play a role in the overall swelling of the jellyroll considering the high achieved pressure. Hence, each component contribution must be studied separately to fully understand the full-cell expansion behaviour and its impact on porosity of the components.

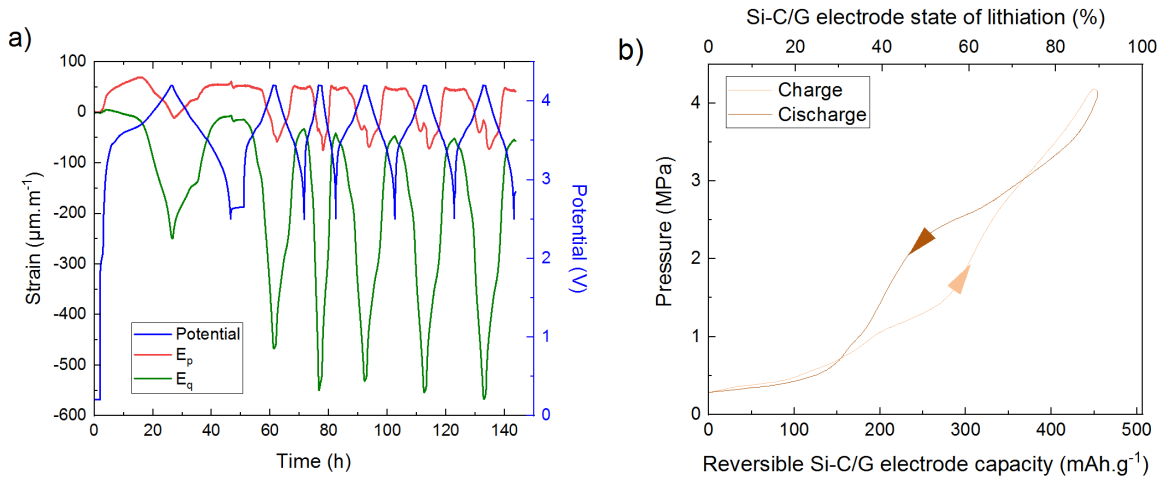

Figure 5 : a) Axial and orthoradial principal strains Ep and Eq during formation protocol at increasing C-rate (C/20, C/10 and C/5) and 3 additional cycles at C/10 - b) Radial pressure of a cylindrical cell vs SOC during 4th cycle at C/10. Radial pressure for each cycle is presented in SI (Figure S7).

2.4.2. 3D image analyses: methodology to determine *in situ* components thickness evolution during one charge discharge cycle

The theoretical anode expansion considering constant pores volume is estimated up to 23.4% (Figure 3), exclusively accommodated inside the hard metal casing of the cylindrical cell. Therefore, an experimental study focusing on each components thickness change during one charge/discharge cycle was performed by using 3D X-ray micro-CT. The obtained reconstructed 3D image required a specific image treatment and analyse procedure using FIJI software to extract quantitative measurements on each components thickness.

At first, the whole 3D volume was processed in order to facilitate data treatment and to ensure the good quality of the 2D slices stack. The reconstructed 3D image being a large data set of 1000 2D slices in 16 bits, the processing on FIJI software was eased by converting it to a set of slices in 8 bits without losing too much detail (Figure S8). Some slices with artefacts were deleted to not locally alter the data (Figure S9). Those came from the 3D image reconstruction step of a small VOI in such a large object surrounded by a dense metal casing. The alignment of all 2D slices along z-axis testifying the 18650 did

not tilt during the data acquisition was confirmed using the orthogonal views tool. No filter was applied to not alter the data.

Next, by looking at the histogram of one slice it was impossible to distinguish five populations of grey level corresponding to the five components of the jellyroll – cathode, anode, Cu and Al current collectors and separator. To overcome this problem, slices representing the average grey level intensity of ~325 slices were created by using the Z-project tool to generate three smaller volumes (Figure S10a). The resulting ortho slice (Figure S10c) is more contrasted and the corresponding histogram exhibits three broad peaks, making it easier to distinguish the five components of the cell (Figure S9b).

A longitudinal profile from a 100 px width line perpendicular to the enrolment was then used to determine the thickness of each component (Figure S10c). The obtained profile (Figure 6) clearly reveals the alternation of the 5 components within the jellyroll (cathode, anode, Cu and Al current collectors and separator). The slight tilt of the profile mean slope coming from high absorption of the components was mathematically corrected. Light grey (GSV above 180) matches the Cu current collector (Cu foil) sandwiched between two layers of anode (GSV between 153 and 156). The other stack corresponds to the Al current collector (grey value between 156 and 160) sandwiched between two layers of cathode (grey values between 166 and 170). Finally, the darkest layers correspond to the separator (grey value below 153). The interface position between two consecutive layers was identified from local maxima of the first derivative of the line-profile with a precision of 1 pixel corresponding to 1.6 µm (Figure S11). The measured thicknesses (between two interfaces) were mathematically corrected considering the Al and Cu current collector incompressible with a steady thickness of 20 µm and 10 µm respectively.

This image and data processing (Z-project and 100 px longitudinal line-profile) is done for each 3 sub-volume, giving numerous measurements of each components thickness for one given SOC. One sub-volume contains an alternation of 5 Cu-collectors, 10 cathodes, 5 Al-collector, 9 anodes and 9 separator). Thus, all following results are average values of multiple measurements with a precision of

1 pixel, i.e. 1.6 µm, and are presented along with the associated standard deviation. This is a way to overcome the relatively large voxel size (1.6 µm) compared to the layer's thicknesses (20-60 µm) and have a representative measurement of the components thicknesses in the overall volume.

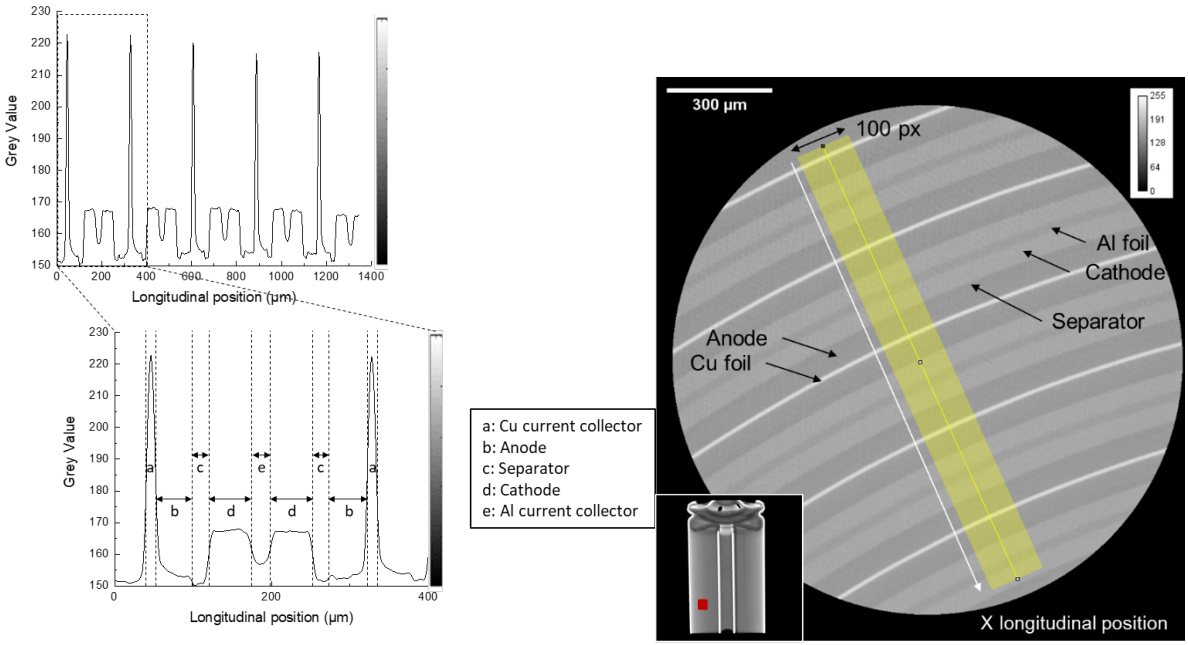

Figure 6: right. Left) Example of longitudinal line-profile obtained from the yellow stripe (width: 100 px); right) Ortho slice obtained from a projection method (Z-project, average pixel intensity) applied on a sub-volume (stack of 325 ortho slices). The sub volume is extracted from a high-resolution scan of the 18650 cylindrical cell at SOC 0% (voxel size of 1.6 µm). The inset shows the position of the VOI selected for high resolution scan.

2.4.3. Components thickness variation during a cycle and resulting effect on porosity

As shown in the study of the hard casing rigidity, the jellyroll experiences first an increase of the maximum pressure during the 3 formation cycles with a most likely increase of the components thickness as there is a necessary initial void in between the jelly roll and the steel case to enable their assembly. Internal components thickness variation was firstly measured by micro-CT after the 3 cycles of formation at 0% SOC for comparison with the initial values measured before assembling using a micrometre (Table 2). No thickness difference was spotted regarding the inner or outer position of the active layer for both anode and cathode.

Table 2: Thickness of bi-layer cathode, bi-layer anode and separator before winding from Lhomargy micrometre measurements with a precision of 1 µm and after 3 formation cycles at SOC 0% from micro-CT measurements with a voxel size of 1.6 µm.

	Cathode	*Anode*	*Separator*
Before assembling	137 ± 1 µm	100 ± 1 µm	20 ± 1 µm
At 0% SOC after 3 formation cycles	134 ± 1.1 µm	106 ± 0.7 µm	20 ± 0.8 µm

At the remaining pressure of 0.3 MPa when discharged, the anode exhibits an irreversible swelling of +6 µm (Table 2). This expansion corresponds to an increase of 6.6% of the active layer thickness compared to the value measured during assembling. Regarding the cathode, a contraction of 3 µm, i.e., 2.5% of active layer, is observed and no significant thickness change can be noted for the separator. So, the irreversible swelling of the anode is compensated equally by the cathode contraction and by filling the void between the jellyroll and the steel case.

Then the reversible swelling of the anode during a charge/discharge cycle, was measured by micro-CT at 8 different SOC (4 in charge and 4 in discharge) for one cycle and is depicted in Figure 7. For anode and cathode, the plotted thickness change is reported considering only one of the 2 active layers of double side coated electrodes, as it will be compared with pouch cells results with single side coated ones, with respectively 45 and 58.5 µm for anode and cathode thicknesses measured during assembling.

The 8 SOC (and corresponding anode SOL) have been chosen from results at constant pressure in the aim to have similar swelling, in particular for the SOC points corresponding to 39% in charge and 27% in discharge, and for those corresponding to 74% in charge and 39% in discharge. The swelling is not that asymmetric between charge and discharge in 18650 cylindrical cell as observed at constant pressure in 0.1 or 1 MPa for pouch cell. More precisely, the anode shows a linear and reversible expansion/contraction process correlated with the lithiation/delithiation electrochemical process. A maximum amplitude of this expansion (+2.3 µm) is measured at 100% SOC or SOL, corresponding to +4.8% compared to the initial thickness measured at the end of 3 formation cycles (0% SOC, Table 2).

The absence of hysteresis between the lithiation and delithiation processes might have two explanations: either voxel size is too large to distinguish the hysteresis, or the constant rise of the pressure up to 4.5 MPa during lithiation leads to different steps in the lithiation/delithiation process of the two components.

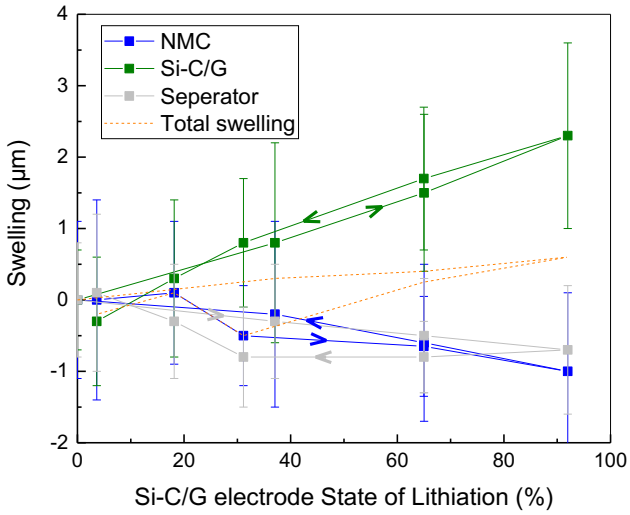

Figure 7: Thickness variation of cylindrical cell internal components (NMC cathode, Si-C/G anode and separator) measured from in situ micro-CT measurements (voxel size: 1.6µm³) upon one cycle of charge/discharge (at 8 various SOL %) at C/10 after formation. Swelling of one active layer is plotted for anode and cathode (not the bi-layer swelling). Total swelling is obtained by summing swelling of each component (anode, cathode, and separator).

In contrast, the cathode and the separator undergo a contraction of -1 µm and -0.8 µm of the initial measured thickness at the end of 3 formation cycles (-1.7% and -4%) respectively which is coherent with values obtained in compression set-up in Figure S6. Their swelling profile is not as linear as the anode one, especially for the separator, showing a slight hysteresis in the process. Cathode contraction comes from both structural changes in the material lattice[33] and mechanical elastic deformation or shrinkage, whereas the separator shrinkage is only a consequence of anode expansion but remains very low, contrary to what was reported for others separators[44,45]. The impact on separator porosity should be a reduction from 39 to 35%. Finally, the sum of all variation is close to zero (Figure 7) which is expected since the whole process takes place in an almost constant volume.

It is important to note here the small swelling amplitude of the anode compared to the swelling amplitude measured for the pouch cells under both 0.1 MPa and 1 MPa (Figure 4). This is certainly a direct consequence of the high pressure applied by the jellyroll during cycling and may have a significant impact on the electrode porosity.

2.5. Impact of internal components deformations on their porosity

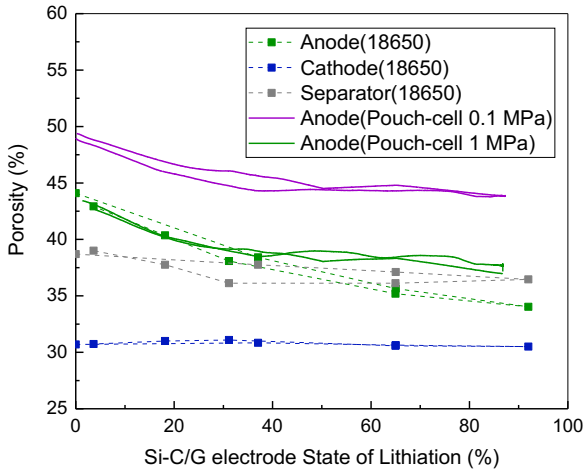

Figure 8: Comparison of the porosity change upon one cycle at C/5 after formation in pouch cell and cylindrical design.

Simple subtraction between the experimental swelling and the theoretical swelling calculated in part 2.2 allows an estimation of the anode pores volume and porosity (equations 7 and 8) presented in Figure 8.

All anode porosities were set to 40% during cell assembly. When assembled in 18650 cylindrical hard casing, the necessary initial void between the jelly roll and the steel case explains the initial 44% anode porosity, while the cathode porosity slightly decreases from 32 to 31% which might be due to remaining pressure of 0.3 MPa in the cell at 0% SOC. The separator has kept its initial porosity of 39%. For the pouch cell cycled under constant pressure of 0.1 MPa and then 1 MPa, the anode porosity has increased to 49% and 44%, respectively. For such cycling conditions, the residual anode porosity appears to be directly linked to the pressure applied during the test. A pressure of 0.1 MPa is not enough to stabilize the anode porosity at 0% SOC after 4 cycles, while 3 cycles at 1 MPa can stabilize it at shown on Figure 4a. Then for these cycling conditions at constant pressure, the porosity slightly

decreases in the first half of the lithiation and remains stable then at 45 and 38% for 0.1 MPa and 1 MPa respectively; for hard casing cell, the anode porosity decreases all along the lithiation. Contraction of the separator and the cathode remains low. While the porosity evolution is similar for the first half of lithiation between anode cycled at a constant pressure of 1 MPa and in hard casing, the final porosity is fairly lower for this last one, with a value of 35%. This confirms the explanation of the higher resistance at 50% SOC for the hard casing cell. The anode porosity is lower which might lower ion mobility and increase charge transfer. Then, during ageing, as the hard casing cell is rigid, SEI accumulation will lead to a reduction of anode porosity while for constant pressure in pouch cell, it might be compensated by a thickness increasing.

3. Conclusion

A system based on the same NMC622 cathode, separator, and Si-C/G anode (having a reversible specific capacity of 500 mAh.g^{-1}) was evaluated at constant volume in 18650 cylindrical casing and in pouch cells under constant pressures of 0.1 and 1 MPa. Results reveal a long lifespan of all cells with more than 80% of the initial capacity after 400 cycles in 18650 casing. Despite a higher capacity loss at the first cycles, cells tested at constant pressures show similar capacity retention after 500 cycles similar to what is observed in hard casing. The highest pressure shows a better capacity retention but also higher resistance at 2C for a 30s pulse.

Swelling of anodes at constant pressure was measured for the initial cycle after formation using an in-house high precision compression set-up. Swelling is directly linked to the state of lithiation of the active materials and is an original way to distinguish the active materials contribution as a function of SOC for a composite anode. The swelling is not symmetric in charge and discharge as silicon is lithiated simultaneously with graphite, while being delithiated after graphite. The test at 0.1 MPa has shown that the pore volume changes at low SOL before reaching a plateau at higher SOL. This pressure was also too low to recover the initial anode porosity of 38% after a cycle. After 4 cycles the remaining porosity at 0% SOC, calculated using a model developed based on Dahn *et al.* works, is ~49%. Then

when applying cycles at 1 MPa, the remaining porosity decreases down to 44% and 38% respectively at 0% and 100% SOC.

High-resolution 3D imaging at micrometre-scale allowed us to distinguish the various components in the rigid 18650 casing and measuring their thickness variation during one charge/discharge cycle despite of the large scale of the cylindrical cell. 8 SOC points were chosen on the electrochemical cycle (4 in charge, 4 in discharge) and the thickness of each component was extracted by using a specific image processing. The 3 layers separator used in this study has a low compression of less than 1µm at 4.5 MPa, the maximum pressure measured in hard casing. Anode has the highest swelling, which is in this case linked to pressure generated by the active materials expansion. Anode assembled in cell at a porosity of 40% with the necessary void between the jelly roll and the rigid casing shows a porosity evolution up to 44% at 0% SOC while a remaining pressure of 0.3 MPa was measured on the casing. The cell charge leads to an anode porosity decrease down to 35% and the active cathode thickness contraction of less than 1 µm.

Upon cycling, while SEI is generated, pores volume should decrease in hard casing, which is not so obvious for constant pressure tests. However electrochemical results did not show any sudden capacity fading or resistance increasing. Our future works will be focused on the estimation of the SEI properties in the anode in order to estimate the remaining porosity after cycling, and electrode and cell design parameters influence, such as initial anode porosity, on the swelling at constant pressure.

Acknowledgments

We gratefully acknowledge funding support from Umicore.

Bibliography

[1] R. Schmuch, R. Wagner, G. Hörpel, T. Placke, M. Winter, Performance and cost of materials for lithium-based rechargeable automotive batteries, Nat. Energy. 3 (2018) 267–278. https://doi.org/10.1038/s41560-018-0107-2.

[2] M. Armand, P. Axmann, D. Bresser, M. Copley, K. Edström, C. Ekberg, D. Guyomard, B. Lestriez, P. Novák, M. Petranikova, W. Porcher, S. Trabesinger, M. Wohlfahrt-Mehrens, H. Zhang, Lithium-ion batteries - current state of the art and anticipated developments, J. Power Sources. (2020) 228708 (26 pp.). https://doi.org/10.1016/j.jpowsour.2020.228708.

[3] M.N. Obrovac, Si-alloy negative electrodes for Li-ion batteries, Curr. Opin. Electrochem. 9 (2018) 8–17. https://doi.org/10.1016/j.coelec.2018.02.002.

[4] Y. Jin, B. Zhu, Z. Lu, N. Liu, J. Zhu, Challenges and Recent Progress in the Development of Si Anodes for Lithium-Ion Battery, Adv. Energy Mater. 7 (2017) 1700715. https://doi.org/10.1002/aenm.201700715.

[5] L.Y. Beaulieu, K.W. Eberman, R.L. Turner, L.J. Krause, J.R. Dahn, Colossal Reversible Volume Changes in Lithium Alloys, Electrochem. Solid-State Lett. 4 (2001) A137. https://doi.org/10.1149/1.1388178.

[6] L.Y. Beaulieu, T.D. Hatchard, A. Bonakdarpour, M.D. Fleischauer, J.R. Dahn, Reaction of Li with Alloy Thin Films Studied by In Situ AFM, J. Electrochem. Soc. 150 (2003) A1457–A1464. https://doi.org/10.1149/1.1613668.

[7] A.J. Louli, J. Li, S. Trussler, C.R. Fell, J.R. Dahn, Volume, Pressure and Thickness Evolution of Li-Ion Pouch Cells with Silicon-Composite Negative Electrodes, J. Electrochem. Soc. 164 (2017) A2689–A2696.

[8] A.J. Louli, L.D. Ellis, J.R. Dahn, Operando Pressure Measurements Reveal Solid Electrolyte Interphase Growth to Rank Li-Ion Cell Performance, Joule. 3 (2019) 745–761. https://doi.org/10.1016/j.joule.2018.12.009.

[9] V. Müller, R.-G. Scurtu, K. Richter, T. Waldmann, M. Memm, M.A. Danzer, M. Wohlfahrt-Mehrens, Effects of Mechanical Compression on the Aging and the Expansion Behavior of Si/C-Composite|NMC811 in Different Lithium-Ion Battery Cell Formats, J. Electrochem. Soc. 166 (2019) A3796–A3805. https://doi.org/10.1149/2.1121915jes.

[10] G. Berckmans, L. De Sutter, M. Marinaro, J. Smekens, J. Jaguemont, M. Wohlfahrt-Mehrens, J. van Mierlo, N. Omar, Analysis of the effect of applying external mechanical pressure on next generation silicon alloy lithium-ion cells, Electrochimica Acta. 306 (2019) 387–395. https://doi.org/10.1016/j.electacta.2019.03.138.

[11] P. Daubinger, F. Ebert, S. Hartmann, G.A. Giffin, Impact of electrochemical and mechanical interactions on lithium-ion battery performance investigated by operando dilatometry, J. Power Sources. 488 (2021) 229457. https://doi.org/10.1016/j.jpowsour.2021.229457.

[12] I. Profatilova, E. De Vito, S. Genies, C. Vincens, E. Gutel, O. Fanget, A. Martin, M. Chandesris, M. Tulodziecki, W. Porcher, Impact of Silicon/Graphite Composite Electrode Porosity on the Cycle Life of 18650 Lithium-Ion Cell, ACS Appl. Energy Mater. 3 (2020) 11873–11885. https://doi.org/10.1021/acsaem.0c01999.

[13] P. Pietsch, D. Westhoff, J. Feinauer, J. Eller, F. Marone, M. Stampanoni, V. Schmidt, V. Wood, Quantifying microstructural dynamics and electrochemical activity of graphite and silicon-graphite lithium ion battery anodes, Nat. Commun. 7 (2016) 1–11. https://doi.org/10.1038/ncomms12909.

[14] V. Vanpeene, A. Etiemble, A. Bonnin, E. Maire, L. Roué, In-situ X-ray tomographic study of the morphological changes of a Si/C paper anode for Li-ion batteries, J. Power Sources. 350 (2017) 18–27. https://doi.org/10.1016/j.jpowsour.2017.03.044.

[15] R. Kumar, P. Lu, X. Xiao, Z. Huang, B.W. Sheldon, Strain-Induced Lithium Losses in the Solid Electrolyte Interphase on Silicon Electrodes, ACS Appl. Mater. Interfaces. 9 (2017) 28406–28417. https://doi.org/10.1021/acsami.7b06647.

[16] A. Mukhopadhyay, B.W. Sheldon, Deformation and stress in electrode materials for Li-ion batteries, Prog. Mater. Sci. 63 (2014) 58–116. https://doi.org/10.1016/j.pmatsci.2014.02.001.
[17] X. Yu, Z. Feng, Y. Ren, D. Henn, Z. Wu, K. An, B. Wu, C. Fau, C. Li, S.J. Harris, Simultaneous Operando Measurements of the Local Temperature, State of Charge, and Strain inside a Commercial Lithium-Ion Battery Pouch Cell, J. Electrochem. Soc. 165 (2018) A1578–A1585. https://doi.org/10.1149/2.1251807jes.
[18] V. Vanpeene, J. Villanova, A. King, B. Lestriez, E. Maire, L. Roué, Dynamics of the Morphological Degradation of Si-Based Anodes for Li-Ion Batteries Characterized by In Situ Synchrotron X-Ray Tomography, Adv. Energy Mater. 9 (2019) 1803947. https://doi.org/10.1002/aenm.201803947.
[19] C.R. Hernandez, A. Etiemble, T. Douillard, D. Mazouzi, Z. Karkar, E. Maire, D. Guyomard, B. Lestriez, L. Roué, A Facile and Very Effective Method to Enhance the Mechanical Strength and the Cyclability of Si-Based Electrodes for Li-Ion Batteries, Adv. Energy Mater. 8 (2018) 1701787. https://doi.org/10.1002/aenm.201701787.
[20] T. Waldmann, S. Gorse, T. Samtleben, G. Schneider, V. Knoblauch, M. Wohlfahrt-Mehrens, A Mechanical Aging Mechanism in Lithium-Ion Batteries, J. Electrochem. Soc. 161 (2014) A1742–A1747. https://doi.org/10.1149/2.1001410jes.
[21] L. Gold, T. Bach, W. Virsik, A. Schmitt, J. Müller, T.E.M. Staab, G. Sextl, Probing lithium-ion batteries' state-of-charge using ultrasonic transmission – Concept and laboratory testing, J. Power Sources. 343 (2017) 536–544. https://doi.org/10.1016/j.jpowsour.2017.01.090.
[22] J. Schindelin, I. Arganda-Carreras, E. Frise, V. Kaynig, M. Longair, T. Pietzsch, S. Preibisch, C. Rueden, S. Saalfeld, B. Schmid, J.-Y. Tinevez, D.J. White, V. Hartenstein, K. Eliceiri, P. Tomancak, A. Cardona, Fiji: an open-source platform for biological-image analysis, Nat. Methods. 9 (2012) 676–682. https://doi.org/10.1038/nmeth.2019.
[23] J.R. Dahn, Phase diagram of Li„C6, Phys. Rev. 44 (1991) 9070–9077.
[24] E. Radvanyi, E.D. Vito, W. Porcher, J. Danet, P. Desbois, J.-F. Colin, S.J.S. Larbi, Study of lithiation mechanisms in silicon electrodes by Auger Electron Spectroscopy, J. Mater. Chem. A. 1 (2013) 4956–4965. https://doi.org/10.1039/C3TA10212B.
[25] M.N. Obrovac, L.J. Krause, Reversible Cycling of Crystalline Silicon Powder, J. Electrochem. Soc. 154 (2007) A103. https://doi.org/10.1149/1.2402112.
[26] M.N. Obrovac, L. Christensen, Structural Changes in Silicon Anodes during Lithium Insertion/Extraction, Electrochem. Solid-State Lett. 7 (2004) A93–A96. https://doi.org/10.1149/1.1652421.
[27] C.L. Berhaut, D.Z. Dominguez, P. Kumar, P.-H. Jouneau, W. Porcher, D. Aradilla, S. Tardif, S. Pouget, S. Lyonnard, Multiscale Multiphase Lithiation and Delithiation Mechanisms in a Composite Electrode Unraveled by Simultaneous Operando Small-Angle and Wide-Angle X-Ray Scattering, ACS Nano. 13 (2019) 11538–11551. https://doi.org/10.1021/acsnano.9b05055.
[28] K.P.C. Yao, J.S. Okasinski, K. Kalaga, J.D. Almer, D.P. Abraham, Operando Quantification of (De)Lithiation Behavior of Silicon–Graphite Blended Electrodes for Lithium-Ion Batteries, Adv. Energy Mater. 9 (2019) 1803380. https://doi.org/10.1002/aenm.201803380.
[29] V. Müller, R.-G. Scurtu, M. Memm, M.A. Danzer, M. Wohlfahrt-Mehrens, Study of the influence of mechanical pressure on the performance and aging of Lithium-ion battery cells, J. Power Sources. 440 (2019) 227148. https://doi.org/10.1016/j.jpowsour.2019.227148.
[30] H.-J. Noh, S. Youn, C.S. Yoon, Y.-K. Sun, Comparison of the structural and electrochemical properties of layered Li[NixCoyMnz]O2 (x = 1/3, 0.5, 0.6, 0.7, 0.8 and 0.85) cathode material for lithium-ion batteries, J. Power Sources. 233 (2013) 121–130. https://doi.org/10.1016/j.jpowsour.2013.01.063.
[31] R. Jung, M. Metzger, F. Maglia, C. Stinner, H.A. Gasteiger, Oxygen Release and Its Effect on the Cycling Stability of LiNixMnyCozO2 (NMC) Cathode Materials for Li-Ion Batteries, J. Electrochem. Soc. 164 (2017) A1361. https://doi.org/10.1149/2.0021707jes.
[32] T.D. Hatchard, J.R. Dahn, In Situ XRD and Electrochemical Study of the Reaction of Lithium with Amorphous Silicon, J. Electrochem. Soc. (2004) A838–A842.

[33] L. de Biasi, A.O. Kondrakov, H. Geßwein, T. Brezesinski, P. Hartmann, J. Janek, Between Scylla and Charybdis: Balancing Among Structural Stability and Energy Density of Layered NCM Cathode Materials for Advanced Lithium-Ion Batteries, J. Phys. Chem. C. 121 (2017) 26163–26171. https://doi.org/10.1021/acs.jpcc.7b06363.
[34] C. Cao, I.I. Abate, E. Sivonxay, B. Shyam, C. Jia, B. Moritz, T.P. Devereaux, K.A. Persson, H.-G. Steinrück, M.F. Toney, Solid Electrolyte Interphase on Native Oxide-Terminated Silicon Anodes for Li-Ion Batteries, Joule. 3 (2019) 762–781. https://doi.org/10.1016/j.joule.2018.12.013.
[35] S. Malmgren, K. Ciosek, M. Hahlin, T. Gustafsson, M. Gorgoi, H. Rensmo, K. Edström, Comparing anode and cathode electrode/electrolyte interface composition and morphology using soft and hard X-ray photoelectron spectroscopy, Electrochimica Acta. 97 (2013) 23–32. https://doi.org/10.1016/j.electacta.2013.03.010.
[36] D. Alliata, R. Kötz, P. Novák, H. Siegenthaler, Electrochemical SPM investigation of the solid electrolyte interphase film formed on HOPG electrodes, Electrochem. Commun. 2 (2000) 436–440. https://doi.org/10.1016/S1388-2481(00)00056-4.
[37] T.M. Fears, M. Doucet, J.F. Browning, J.K.S. Baldwin, J.G. Winiarz, H. Kaiser, H. Taub, R.L. Sacci, G.M. Veith, Evaluating the solid electrolyte interphase formed on silicon electrodes: a comparison of ex situ X-ray photoelectron spectroscopy and in situ neutron reflectometry, Phys. Chem. Chem. Phys. 18 (2016) 13927–13940. https://doi.org/10.1039/C6CP00978F.
[38] V. Vanpeene, J. Villanova, J.-P. Suuronen, A. King, A. Bonnin, J. Adrien, E. Maire, L. Roué, Monitoring the morphological changes of Si-based electrodes by X-ray computed tomography: A 4D-multiscale approach, Nano Energy. 74 (2020) 104848. https://doi.org/10.1016/j.nanoen.2020.104848.
[39] X. Wang, Y. Sone, S. Kuwajima, In Situ Investigation of the Volume Change in Li-ion Cell with Charging and Discharging: Satellite Power Applications, J. Electrochem. Soc. 151 (2004) A273. https://doi.org/10.1149/1.1635827.
[40] L.K. Willenberg, P. Dechent, G. Fuchs, D.U. Sauer, E. Figgemeier, High-Precision Monitoring of Volume Change of Commercial Lithium-Ion Batteries by Using Strain Gauges, Sustainability. 12 (2020) 557. https://doi.org/10.3390/su12020557.
[41] L. Willenberg, P. Dechent, G. Fuchs, M. Teuber, M. Eckert, M. Graff, N. Kürten, D.U. Sauer, E. Figgemeier, The Development of Jelly Roll Deformation in 18650 Lithium-Ion Batteries at Low State of Charge, J. Electrochem. Soc. 167 (2020) 120502. https://doi.org/10.1149/1945-7111/aba96d.
[42] L. Zolin, M. Chandesris, W. Porcher, B. Lestriez, An Innovative Process for Ultra-Thick Electrodes Elaboration: Toward Low-Cost and High-Energy Batteries, Energy Technol. 7 (2019). https://doi.org/10.1002/ente.201900025.
[43] Y. Jiang, C. Zhang, W. Zhang, W. Shi, Q. Liu, Modeling charge polarization voltage for large lithium-ion batteries in electric vehicles, J. Ind. Eng. Manag. 6 (2013) 686–697. https://doi.org/10.3926/jiem.895.
[44] V.A. Sethuraman, N. Van Winkle, D.P. Abraham, A.F. Bower, P.R. Guduru, Real-time stress measurements in lithium-ion battery negative-electrodes, J. Power Sources. 206 (2012) 334–342. https://doi.org/10.1016/j.jpowsour.2012.01.036.
[45] D. Sauerteig, N. Hanselmann, A. Arzberger, H. Reinshagen, S. Ivanov, A. Bund, Electrochemical-mechanical coupled modeling and parameterization of swelling and ionic transport in lithium-ion batteries, J. Power Sources. 378 (2018) 235–247. https://doi.org/10.1016/j.jpowsour.2017.12.044.